Research Paper

# Unified mechanistic model for Standard SCR, Fast SCR, and NO$_2$ SCR over a copper chabazite catalyst

M. Bendrich[a,b], A. Scheuer[b], R.E. Hayes[a], M. Votsmeier[b,c,*]

[a] University of Alberta, 116 Street, Edmonton, Alberta, T6G 2V4, Canada
[b] Umicore AG & Co. KG, Rodenbacher Chaussee 4, 63457 Hanau, Germany
[c] Technische Universität Darmstadt, Alarich-Weiss-Str. 8, 64287 Darmstadt, Germany
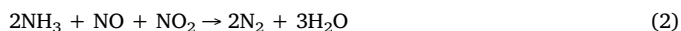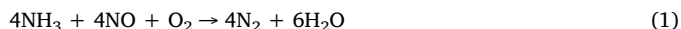
A B S T R A C T

Mechanistic proposals for the different SCR subreactions are integrated into one surface reaction mechanism that describes the main SCR reactions (Standard SCR, Fast SCR, NO$_2$ SCR), transient effects due to nitrate storage, as well as the production of the side product N$_2$O over a copper chabazite catalyst. The mechanism is parameterised to steady state and transient experiments, and is shown to predict the behaviour of the catalyst during a driving cycle, without any refitting of kinetic parameters.

A dual site approach is used, where site 1 accounts for the adsorbed ammonia that forms on the Brønsted acid sites and copper ions, while site 2 is a copper ion (Cu$^{2+}$-OH) where nitrites and nitrates are adsorbed. All main SCR reactions proceed *via* a reaction between ammonia and nitrites (ammonium nitrite pathway) to produce nitrogen; nitrites are also the linking species between the Standard SCR and NO oxidation reactions. Reactions between nitrates and ammonia to produce ammonium nitrate are also included, along with ammonium nitrate decomposition pathways (i.e., *via* NO addition to feed). Additionally, a global reaction taking place between adsorbed ammonia and gaseous NO$_2$ to produce N$_2$ at low temperatures (< 250 °C) is added, to account for an observed reaction taking place on the copper-free zeolite.

The mechanism was used to analyse the importance of nitrate formation during a standard driving cycle. Surprisingly, although a significant amount of inhibitive ammonium nitrate is modelled to form during low temperature Fast and NO$_2$ SCR steady state experiments, almost no ammonium nitrate is predicted to form during the driving cycle, thus allowing for a higher reaction activity than predicted based on steady state data. From a modelling and catalyst testing perspective, this shows the importance of capturing the catalyst's transient behaviour rather than only steady state conditions, since steady state is not necessarily reached during practical driving scenarios.
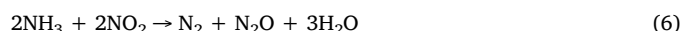
## 1. Introduction

Selective catalytic reduction (SCR) is used in the automotive industry to reduce NO$_x$ gases. In the SCR process, ammonia, the reducing agent, is generated onboard through the hydrolysis of urea. The ratio of NO to NO$_2$ in the exhaust gas entering the SCR catalytic converter affects the selectivity of the main reactions, which are Standard SCR (1), Fast SCR (2), and NO$_2$ SCR (3) [1,2].

$$4NH_3 + 4NO + O_2 \rightarrow 4N_2 + 6H_2O \tag{1}$$

$$2NH_3 + NO + NO_2 \rightarrow 2N_2 + 3H_2O \tag{2}$$

$$4NH_3 + 3NO_2 \rightarrow 3.5\,N_2 + 6H_2O \tag{3}$$

Side reactions such as ammonia oxidation (4) and NO oxidation/

NO$_2$ decomposition (5) at high temperatures (i.e., > 400 °C) [3,4], or ammonium nitrate formation at low temperatures (i.e., < 200 °C), leading to N$_2$O formation [5,6], can also occur.

$$4NH_3 + 3O_2 \rightarrow 2N_2 + 6H_2O \tag{4}$$

$$NO + 0.5O_2 \leftrightarrow NO_2 \tag{5}$$

$$2NH_3 + 2NO_2 \rightarrow N_2 + N_2O + 3H_2O \tag{6}$$

Several catalysts have been used for the automotive SCR. Vanadium catalysts were first implemented because of their use in stationary deNOx applications [7], however, Fe- and Cu-zeolite catalysts became a popular choice owing to requirements for a higher activity at low temperatures and a greater stability at higher temperatures [3]. Recently, catalysts based on copper chabazite (CHA) structures have been

commercialized, which have a smaller pore-structure compared to Cu-ZSM-5 and Cu-BEA [8].

As a result, there has been a significant amount of research published on Cu-CHA catalysts, which led to the identification of possible active sites and the development of mechanisms for the different reactions [9]. The purpose of the current work is to integrate this existing knowledge into a comprehensive model that captures the different subreactions as well as transient effects due to nitrate storage.

In terms of research on the active sites, it has been proposed that $Cu^{2+}$ is found in the CHA's 6-membered ring and at higher loadings, Cu species can be found in some form of $Cu_xO_y$ in the 8-membered ring [10–12]. Both the copper sites and Brønsted acid sites are responsible for ammonia adsorption, but ammonia stored on copper is significantly more reactive in SCR [13,14], whereas the Brønsted sites mainly act as ammonia storage sites [11].

Various mechanistic pathways have been proposed to describe the main SCR reactions (1, 2, 3). While it was originally believed that the oxidation of NO to $NO_2$ (5) is the rate limiting step that connects Standard SCR (1) to Fast SCR (2) [15], evidence by Ruggeri et al. points to nitrite-like species being the linking intermediate between NO oxidation and Standard SCR over zeolites [16–18]. Kwak et al. also proposed that $NO^+$ and not $NO_2$ is an intermediate over a chabazite catalyst, and presented a catalytic cycle for Standard SCR where NO is responsible for the reduction of $Cu^{2+}$, and oxygen is responsible for the re-oxidation [19]. Several catalytic cycles have been proposed for Standard SCR only [20–22] or Standard and Fast SCR [23] over Cu-CHA. $NO_2$ SCR is not captured by these proposed cycles. Nevertheless, there have been separate mechanisms proposed to describe Fast SCR [24,25] and $NO_2$ SCR [26] on Fe-zeolite catalysts.

Fewer papers have focused on the simulation of SCR over Cu-CHA catalysts. A global Cu-CHA model by Olsson et al. [27] used three active sites to predict the behaviour of ammonia adsorption, ammonia oxidation, Standard SCR to $N_2$, and Standard SCR to $N_2O$; the study focused on $NH_3$–NO feeds, thus no $NO_2$ was included. To compare Cu-CHA to Fe-ZSM-5 and combined Fe- and Cu- catalysts, Metkar et al. [28], implemented a global, single site model for Cu-CHA that could predict the steady state conversions for different $NO_2/NO_x$ ratios. One active site was used for ammonia adsorption. The model could simulate the steady state conversions for ammonia oxidation to $N_2$, NO oxidation, Standard SCR to $N_2$, Fast SCR to $N_2$, $NO_2$ SCR to $N_2$, and $NO_2$ SCR to $N_2O$, with ammonium nitrate gas species as an intermediate.

The formation of nitrates and nitrites may lead to additional transient effects that are not captured in models that use ammonia as the only stored species [6]. For instance, ammonium nitrate formation leads to significant low temperature dynamics. This issue is particularly important for Cu-CHA, since owing to the smaller pore size, ammonium nitrate is more stable on Cu-CHA compared to its larger-pore counterparts (i.e., Cu-BEA) [5]. In this work, we integrated mechanistic information and pathways published in the literature to develop a surface reaction mechanism that captures the transients related to mixed $NH_3$–NO/$NO_2$ feeds for Cu-CHA. The mechanism relies on a dual site approach, where one active site is responsible for ammonia adsorption, while the other accounts for the formation of nitrites and nitrates. The kinetic parameters of the reactions were fit to steady state and transient experiments, and model Standard SCR, Fast SCR, and $NO_2$ SCR conditions as well as side reactions such as ammonia oxidation and ammonium nitrate formation, storage, and decomposition. In a final step, the model is used to simulate a driving cycle without refitting of the kinetic parameters. Comparison of the simulated surface species formed during the driving cycle versus steady state experiments indicates that the steady state conditions are not reached during the driving cycle, and emphasizes the importance of modelling transients rather than only steady state activity.

## 2. Methods

### 2.1. Laboratory reactor measurements

The experiments were completed with a commercial, state-of-the-art, copper chabazite catalyst with a commercial copper loading supported on a cordierite substrate. The monolith samples had the following properties: 2.5 cm diameter, 5.1 cm length, cell density of 400 cpsi, and a wall thickness of 109 μm. The samples were aged in a flow of 10% $O_2$ and 10% $H_2O$ with $N_2$ as the balance gas for 16 h at 750 °C. Additionally, a Cu-free, zeolite catalyst sample was used. This sample had 78% of the zeolite content of the Cu-CHA sample, and it was aged for 16 h at 700 °C.

The monolith sample was placed inside a quartz tube through which the feed gas of selected composition and temperature was passed. A thermocouple monitored the inlet gas temperature, which was recorded and is used throughout this paper; outlet temperatures were not recorded, however investigations on the experimental set-up show a maximum temperature difference of 4 °C. The outlet gas composition was measured by an FTIR. The tubing from the reactor to the FTIR was heated to 185 °C to avoid ammonium nitrate deposition.

Three experiment types were used: steady state, transient temperature programmed desorption (TPD), and temperature programmed surface reaction (TPSR). All experiments had 5% $H_2O$ and 6% $O_2$, with $N_2$ as the balance gas, and began with a pre-treatment to ensure that no species were adsorbed on the catalyst. Likewise, the gas hourly space velocity (GHSV) for all experiments was 50,000 $h^{-1}$ at STP, with the exception of the Fast SCR experiments being completed at 125,000 $h^{-1}$ at STP.

For the steady state experiments, the gas of desired composition and temperature was passed over the monolith until steady state was reached, at which point the steady state outlet composition and temperature were recorded. To capture the transient dynamics, TPD experiments were used to determine the ammonia and $NO_2$ adsorption/desorption properties. In this experiment, the desired species were added at a given temperature. As the species were adsorbed by the catalyst, a dead-time was first exhibited, followed by a rapid increase in the outlet concentration after the active sites have been filled. Once the outlet concentration had reached steady state, the species were no longer added to the feed, allowing for any desorption of loosely bound species. A temperature ramp followed, allowing for the desorption of the remaining species. The transient TPSR experiments were similar to the TPD experiments, only multiple species were added in various orders, to allow for a reaction between desired species.

### 2.2. Engine test bench measurement

A WHTC driving cycle was performed on an engine test bench using a Cu-CHA catalyst. The Cu-CHA monolith used at the engine test bench had the following properties: 24.1 cm diameter, 34.3 cm length, cell density of 400 cpsi, and a wall thickness of 74 μm. The catalytic converter was aged in 10% $O_2$ and 10% $H_2O$, with $N_2$ as the balance gas for 16 h at 750 °C.

The engine test bench catalytic converter system consisted of a diesel oxidation catalyst (DOC), a diesel particle filter (DPF), and the SCR catalyst. There was no ammonia initially stored on the SCR catalyst. The aqueous urea solution was injected between the DPF and SCR based on an $NH_3/NO_x$ constant dosing strategy ratio of 1.2. No urea dosing restriction was in place since the temperature of the WHTC driving cycle, which started at an initial temperature of 200 °C rather than a cold start, was always above 180 °C. An FTIR, CLD, and oxygen sensor measured the outlet composition.

## 3. Models

### 3.1. Reactor model

The reactor model assumes that all channels, their washcoat distribution, and the inlet conditions to each channel are identical, allowing one to model a single channel. 1D mass and energy balances are solved for the species in the gas phase and washcoat, where axial advection in the gas phase, mass and heat transfer from the gas phase to washcoat, and source terms from the reactions in the washcoat are included. The position dependent mass and heat transfer coefficients are calculated *via* a Nu and Sh correlation for laminar flow [30]. Internal mass transfer in the washcoat is not explicitly accounted for, and therefore the kinetic parameters may include diffusion effects. The channel was discretized axially, and the mass and energy balances were integrated using DASSL [31]. For a detailed description of the 1D mass and energy balances used, please refer to Opitz et al. [32].

### 3.2. Kinetic model

The model incorporates mechanistic pathways proposed in literature, including the $NO_2$ disproportionation/oxidation mechanism [33,29,17], ammonium nitrate formation on both Brønsted and $Cu^{2+}$ sites [34,29], Standard SCR and NO oxidation mechanism *via* a nitrite route [19,16], Fast SCR [25,24], and $NO_2$ SCR [26]. No reaction is a linear combination of others, and each global SCR reaction can only be described by one linear combination of the mechanistic equations. One exception arises with NO oxidation, which is explained later. The linear combination of the proposed reactions required to model the main global reactions are presented in the Results & Discussions section.

It is assumed that the mechanism takes place on two different active sites: a site where all adsorbed ammonia is stored (*) and a copper site ($Cu^{2+}$-OH/$Cu^+$) that interacts with $NO_2$ and NO. Although it has been proposed that ammonia adsorbs on at least both Brønsted acid and copper sites [13,14], for simplicity, all adsorbed ammonia has been grouped and it was assumed that ammonia adsorption only occurs on one site type; nevertheless, the addition of a Temkin isotherm to describe ammonia desorption reaction equation accounts for the ammonia desorption behaviour on multiple sites [27]. Additionally, rather than distinguishing between monomeric and dimeric copper, it is assumed that the 5% $H_2O$ present in all experiments would cause the monomeric $Cu^{2+}$ and dimers to form $Cu^{2+}$-OH [10,17]. Finally, given that the $H_2O$ (5%) and $O_2$ (6%) added throughout all laboratory reactor experiments was constant, the kinetic dependence of $H_2O$ and $O_2$ is not always included in the rate expressions. The reaction scheme implemented is listed in Table 1, as well as shown as a catalytic cycle in Fig. 1, and the reactions and their role in the mechanism are described in the Results & Discussions section

The rate expressions are also included in Table 1, where $k_f$ and $k_b$ represent the forward and reverse rate constants, respectively, which are described by the Arrhenius Eq. (7). In Eq. (7), *A* is the pre-exponential factor, *E* is the activation energy, *R* is the gas constant and *T* is the temperature.

$$k = A \exp(-E/RT) \tag{7}$$

The surface coverages related to the ammonia storage site (*) include $\theta_V$ (vacent sites), $\theta_{NH3}$ (ammonia), $\theta_{NH4NO3}$ (ammonium nitrate); the surface coverages related to the copper site ($Cu^{2+}$/$Cu^+$) include $\sigma_{OH}$ ($Cu^{2+}$-OH), $\sigma_{ONO}$ (nitrites), $\sigma_{NO3}$ (nitrates), $\sigma_{NO3NH3}$ (blocking species), $\sigma_{Cu+}$ (reduced copper). The sum of the surface coverages on each site equals one.

The pre-exponential factors and activation energies of each reaction were fitted to the steady state and transient experiments. The optimization algorithm used was gradient-based algorithm for a constrained, non-linear problem and the starting points were user defined.

## 4. Results & discussions

### 4.1. Adsorption of ammonia

Ammonia TPD experiments were completed to capture the ammonia adsorption-desorption dynamics. Adsorption temperatures of 150, 200, and 250 °C were used, and the results from the experiment at 150 °C are shown in Fig. 2. A feed of 500 ppm $NH_3$ with 5% $H_2O$ and 6% $O_2$, with $N_2$ as the balance gas was passed through the catalytic converter. Initially, ammonia was adsorbed, followed by ammonia breakthrough after the active sites have been filled to their equilibrium amount (time: 0–3400 s). Once steady state was reached, ammonia was discontinued in the feed, resulting in the desorption of ammonia (time: 3400–4400 s). Starting at 4400 s, the temperature was gradually increased (10 K/min), which resulted in further desorption of ammonia (time: 4400–6600 s).

At 150 °C and 200 °C, all of the adsorbed ammonia was recovered during the desorption, within an error tolerance. The experimental percent difference between the amount of ammonia adsorbed and desorbed (physical desorption and during temperature ramp) was 2% at 150 °C and 3% at 200 °C. The percent difference increased at higher adsorption temperatures due to ammonia oxidation, and thus the nitrogen balance could no+ longer be closed at 250 °C (22% nitrogen deficit).

The pre-exponential factor and activation energy of Equation R1r (r = reverse reaction), along with the ammonia site density, was fit using the three ammonia TPD experiments; the resulting fit is shown in Fig. 2. The adsorption and physical desorption is well-predicted, whereas there is a slight discrepancy between the experimental and simulated ammonia desorption during the temperature ramp. The addition of a second ammonia adsorption site would help improve this fit, which has been avoided here for simplicity.

### 4.2. Formation of nitrites and nitrates via $NO_2$ adsorption

In oxidative conditions, $NO_2$ adsorption is understood to proceed *via* a disproportionation/oxidation mechanism [33,29,17]. This mechanism has been included in this model as R2 to R4, whose linear combination describes the global $NO_2$ adsorption equation (Table 2), and R5 accounting for the desorption of $NO_2$ at higher temperatures.

To investigate $NO_2$ adsorption, $NO_2$ TPD experiments were completed with adsorption temperatures of 150, 200, and 250 °C. The experiments performed at 150 and 250 °C, and the simulations are shown in Fig. 3. At the beginning of the experiment, 500 ppm $NO_2$ passed through the catalytic converter sample (Fig. 3**A, C**). During this stage, $NO_2$ was adsorbed as nitrates and nitrites (R2 and R3), where nitrites were oxidized *via* $NO_2$ to produce NO and nitrates (R4). Thereafter, the $NO_2$ approached equilibrium conditions with the nitrates, NO, and $HNO_3$, owing to R2, R3r, and R4. Thus, the $NO_2$ consumption, NO produced (6 ppm at 150 °C; 3 ppm at 250 °C), and nitric acid ($HNO_3$) produced (9 ppm at 150 °C; 5 ppm at 250 °C) reached steady state. More nitrates were stored at lower temperatures, which also resulted in more NO and $HNO_3$ being produced. The nitrites acted as a steady state intermediate, where the nitrites produced were always automatically consumed. Once $NO_2$ had reached steady state, $NO_2$ was eliminated from the feed (not shown); the temperature of the feed gas was then increased, where $HNO_3$ and $NO_2$ were produced from the stored nitrates *via* R3r (r = reverse reaction) and R5 (Fig. 3**B, D**). Throughout the entire experiment, 5% $H_2O$, 6% $O_2$, and $N_2$ as the balance gas was included in the feed.

The stoichiometry of the global $NO_2$ adsorption equation (Table 2), shows that for every three $NO_2$ consumed, two nitrates and one NO are produced. This ratio of $NO_2$ to NO was observed during the adsorption phase of all the $NO_2$ adsorption experiments (3.3:1 at 150 °C, 3.2:1 at 200 °C, 3.0:1 at 250 °C). Nitrogen balances were completed over the length of the three $NO_2$ TPD experiments, with $NO_2$, NO, and $HNO_3$

**Table 1**
Reaction mechanism.

| Reaction | | Rate Expression |
|---|---|---|
| R1 | $NH_3 + * \leftrightarrow NH_3*$ | $A_f \cdot c_{NH3} \cdot \theta_V - A_b \exp\left(\frac{-E(1-\gamma \cdot \theta_{NH3})}{RT}\right) \cdot \theta_{NH3}$ |
| R2 | $2NO_2 + Cu^{2+} - OH \leftrightarrow Cu^{2+} - ONO + HNO_3$ | $k_f \cdot c_{NO2}^2 \cdot \sigma_{OH} - k_b \cdot c_{HNO3} \cdot \sigma_{ONO}$ |
| R3 | $HNO_3 + Cu^{2+} - OH \leftrightarrow Cu^{2+} - NO_3 + H_2O$ | $k_f \cdot c_{HNO3} \cdot \sigma_{OH} - k_b \cdot \sigma_{NO3}$ |
| R4 | $NO_2 + Cu^{2+} - ONO \leftrightarrow Cu^{2+} - NO_3 + NO$ | $k_f \cdot c_{NO2} \cdot \sigma_{ONO} - k_b \cdot c_{NO} \cdot \sigma_{NO3}$ |
| R5 | $Cu^{2+} - NO_3 + H_2O \rightarrow NO_2 + \frac{1}{4}O_2 + Cu^{2+} - OH$ | $k_f \cdot \sigma_{NO3}$ |
| R6 | $Cu^{2+} - ONO + NH_3* \rightarrow N_2 + H_2O + Cu^{2+} - OH + *$ | $k_f \cdot \sigma_{ONO} \cdot \theta_{NH3}$ |
| R7 | $Cu^{2+} - ONO + NH_3* + \frac{1}{2}O_2 \rightarrow N_2O + H_2O + Cu^{2+} - OH + *$ | $k_f \cdot \sigma_{ONO} \cdot \theta_{NH3}$ |
| R8 | $3Cu^{2+} - NO_3 + 2NH_3* \rightarrow 3Cu^{2+} - ONO + N_2 + 3H_2O + 2*$ | $k_f \cdot \sigma_{NO3} \cdot \theta_{NH3}$ |
| R9 | $Cu^{2+} - NO_3 + NH_3* \leftrightarrow Cu^{2+} - NO_3[NH_3] + *$ | $k_f \cdot \sigma_{NO3} \cdot \theta_{NH3} - k_b \cdot \sigma_{NO3NH3} \cdot \theta_V$ |
| R10 | $Cu^{2+} - NO_3[NH_3] \rightarrow N_2O + H_2O + Cu^{2+} - OH$ | $k_f \cdot \sigma_{NO3NH3}$ |
| R11 | $Cu^{2+} - NO_3[NH_3] + * + H_2O \leftrightarrow NH_4NO_3* + Cu^{2+} - OH$ | $k_f \cdot \sigma_{NO3NH3} \cdot \theta_V - k_b \cdot \theta_{NH4NO3} \cdot \sigma_{OH}$ |
| R12 | $2Cu^{2+} - OH + NO \leftrightarrow Cu^{2+} - ONO + H_2O + Cu^+$ | $k_f \cdot c_{NO} \cdot \sigma_{OH} - k_b \cdot \sigma_{ONO} \cdot \sigma_{Cu+}$ |
| R13 | $Cu^+ + \frac{1}{2}H_2O + \frac{1}{4}O_2 \rightarrow Cu^{2+} - OH$ | $k_f \cdot c_{O2}^\alpha \cdot \sigma_{Cu+}$ |
| R14 | $Cu^{2+} - ONO + \frac{1}{2}H_2O + \frac{1}{4}O_2 \leftrightarrow NO_2 + Cu^{2+} - OH$ | $k_f \cdot \sigma_{ONO} - k_b \cdot c_{NO2} \cdot \sigma_{OH}$ |
| R15 | $4NH_3* + 5O_2 \rightarrow 4NO + 6H_2O + 4*$ | $k_f \cdot c_{O2}^\alpha \cdot \theta_{NH3}$ |
| R16 | $2NH_3* + 2O_2 \rightarrow N_2O + 3H_2O + 2*$ | $k_f \cdot c_{O2}^\alpha \cdot \theta_{NH3}$ |
| R17 | $2Cu^{2+} - NO_3 + 2NH_3* \rightarrow N_2 + 2NO + 2H_2O + 2Cu^{2+} - OH + 2*$ | $k_f \cdot \sigma_{ONO} \cdot \theta_{NH3}$ |
| R18 | $2NH_3* + 2NO_2 \rightarrow 2N_2 + 3H_2O + \frac{1}{2}O_2 + 2*$ | $k_f \cdot c_{NO2} \cdot \theta_{NH3}$ |

species being accounted for; $HNO_3$, which is rarely reported, was crucial to closing the nitrogen balance. The nitrogen balances resulted in higher errors at lower temperatures, where more nitrogen was adsorbed than desorbed. The percent differences were 14% at 150 °C, 6% at 200 °C, and −3% at 250 °C.

The $Cu^{2+}$-OH site density, pre-exponential factors, and activation energies of R2 to R5 were fit using the three $NO_2$ TPD experiments. The resulting kinetic fit shown in Fig. 3 describes the reactions well. To validate the $NO_2$ adsorption kinetic fit, an $NO_2$–NO TPSR experiment was completed at an adsorption temperature of 150 °C, where the experiment is shown in Fig. 4. In this experiment, NO was added after $NO_2$ adsorption, where the addition of NO removes the nitrates from the catalyst surface and produces $NO_2$ (R4r, R3r, R2r). Thereafter, NO was eliminated from the feed, and the temperature of the feed gas was increased at a rate of 20 K/min (not shown); no $NO_2$, NO, or $HNO_3$ was detected, indicating that all nitrates had been removed from the surface during the NO addition. The kinetic model captured these effects via the reverse reaction shown in Table 2; however, the experimental ratio of $NO_2$ to NO was 2.2:1 rather than 3:1. This observation is similar to



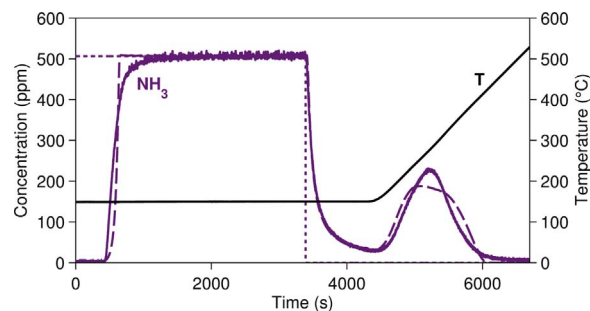**Fig. 2.** Ammonia TPD experiment (solid line) and simulation (dashed line) with adsorption temperature of 150 °C; Feed (dotted line) = 0/500 ppm $NH_3$, 5% $H_2O$, 6% $O_2$, $N_2$ as Balance Gas; GHSV at STP = 50,000 $h^{-1}$.
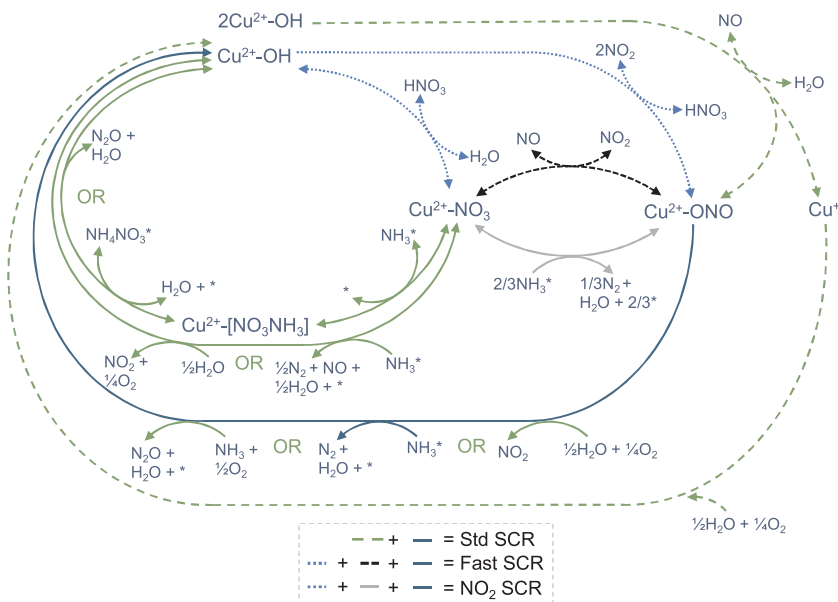
**Fig. 1.** Reaction mechanism as catalytic cycle.

**Table 2**
Linear reaction combination for $NO_2$ adsorption.

| | |
|---|---|
| **R2** | $2NO_2 + Cu^{2+} - OH \leftrightarrow Cu^{2+} - ONO + HNO_3$ |
| **R3** | $HNO_3 + Cu^{2+} - OH \leftrightarrow Cu^{2+} - NO_3 + H_2O$ |
| **R4** | $NO_2 + Cu^{2+} - ONO \leftrightarrow Cu^{2+} - NO_3 + NO$ |
| **Sum:** | $\mathbf{3NO_2 + 2Cu^{2+} - OH \leftrightarrow 2Cu^{2+} - NO_3 + NO + H_2O}$ |

Grossale et al. [34], indicating that the oxidation-reduction of copper may play a role [6], which is not investigated in detail here.

### 4.3. NO oxidation, $NO_2$ decomposition, and standard SCR via a nitrite pathway

The Standard SCR mechanism has yet to be agreed upon, where points of debate have been well-documented in a copper chabazite review by Beale et al. [9]. Beale et al. summarizes these points as: (1) whether SCR takes place as a redox reaction, (2) the role of ammonia stored on Brønsted acid versus copper sites, (3) the role of $NO_2$ in the SCR mechanism, (4) monomeric versus dimeric copper [9]. Recent literature published for Cu-CHA shows that redox of $Cu^{2+}/Cu^+$ plays a role in Standard SCR [35,21], and that ammonia stored on copper is significantly more reactive in SCR than on the Brønsted acid sites, which are responsible for ammonia storage [14,13,11]. Although $NO_2$ was initially proposed as an intermediate in Standard SCR over zeolites [15], there has been a significant amount of support showing that this is not possible. Rather, a nitrite-like species is proposed to be the intermediate [19,18,16]. Such a nitrite-like species has also been suggested to be the linking intermediate to NO oxidation [18,16].

Given the evidence of $Cu^{2+}/Cu^+$ cycling and the linking intermediate in SCR and NO oxidation being nitrite-like species, the main reactions implemented here for Standard SCR and NO oxidation account for these features. Likewise, although all ammonia stored in this mechanism is assumed to be on a single site, ammonia adsorption on the copper and Brønsted acid sites has been captured via the addition of the Temkin isotherm in the ammonia desorption rate equation (R1). No distinction has been made between the copper species (monomeric versus dimeric); however, since 5% $H_2O$ is always present in the feed, it is possible that monomeric $Cu^{2+}$ would be of the form $Cu^{2+}$-OH [10] while the equilibrium of a copper dimer in a water feed would shift to also form $Cu^{2+}$-OH [17].

The implemented reactions for Standard SCR and NO oxidation are based on nitrite-pathways proposed by Ruggeri et al. and Kwak et al.
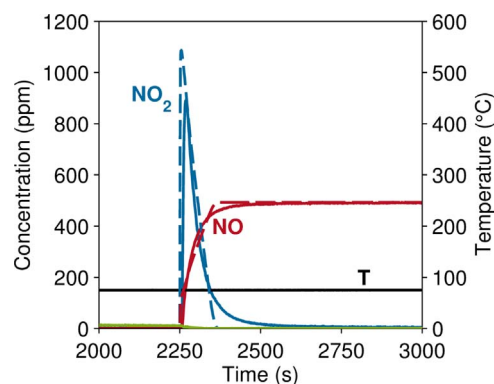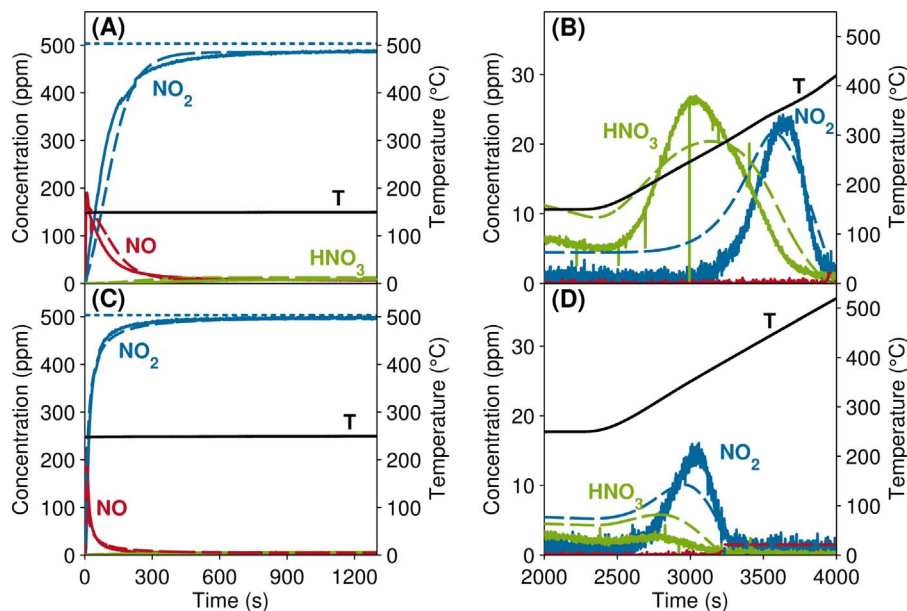


**Fig. 4.** $NO_2$–NO TPSR experiment (solid lines) and simulation (dashed lines) with adsorption temperature of 150 °C; Feed (dotted lines) = 0 ppm $NO_2$, 500 ppm NO, 5% $H_2O$, 6% $O_2$, $N_2$ as Balance Gas; GHSV at STP = 50,000 $h^{-1}$. Catalyst was pretreated with 500 ppm $NO_2$ for 25 min beforehand to allow for nitrate storage.

**Table 3**
Linear reaction combination for Standard SCR.

| | |
|---|---|
| **4\*R1** | $4NH_3 + 4^* \leftrightarrow 4NH_3^*$ |
| **4\*R12** | $8Cu^{2+} - OH + 4NO \leftrightarrow 4Cu^{2+} - ONO + 4H_2O + 4Cu^+$ |
| **4\*R6** | $4Cu^{2+} - ONO + 4NH_3^* \rightarrow 4N_2 + 4H_2O + 4Cu^{2+} - OH + 4^*$ |
| **4\*R13** | $4Cu^+ + 2H_2O + O_2 \rightarrow 4Cu^{2+} - OH$ |
| **Sum:** | $\mathbf{4NH_3 + 4NO + O_2 \rightarrow 4N_2 + 6H_2O}$ |

[16,19]. Although many Standard SCR mechanisms have been published as catalytic cycles with various intermediate species [23,20–22], we opted to maintain as simple of a mechanism as possible with few intermediates, and found our current implementation simulates Standard SCR well. In this work, Standard SCR is described via a combination of R1, R12, R6, and R13 (Table 3). The global unselective Standard SCR to $N_2O$ can be described by replacing R6 in Table 3 with R7.

In Table 3, Reaction R12 represents the reduction of $Cu^{2+}$ by NO, resulting in $Cu^+$ and a nitrite species on $Cu^{2+}$. The nitrites react with ammonia to produce nitrogen and water via an ammonium nitrite route (R6) while the reduced $Cu^+$ sites become re-oxidized via oxygen (R13). While recent DFT-based mechanistic proposals suggest the re-oxidation of $Cu^+$ proceeds via both NO and $O_2$ [21,23], for simplicity, $Cu^+$ is modelled to only be re-oxidized using $O_2$ and $H_2O$. Since re-oxidation



**Fig. 3.** $NO_2$ TPD experiment (solid lines) and simulation (dashed lines) with adsorption temperature of 150 °C (A, B) and 250 °C (C, D); Feed (dotted lines) = 0/500 ppm $NO_2$, 5% $H_2O$, 6% $O_2$, $N_2$ as Balance Gas; GHSV at STP = 50,000 $h^{-1}$.

**Table 4**
Linear reaction combination added for NO oxidation.

| | |
|---|---|
| **R12** | $2Cu^{2+} - OH + NO \leftrightarrow Cu^{2+} - ONO + H_2O + Cu^+$ |
| **R14** | $Cu^{2+} - ONO + \frac{1}{2}H_2O + \frac{1}{4}O_2 \leftrightarrow NO_2 + Cu^{2+} - OH$ |
| **R13** | $Cu^+ + \frac{1}{2}H_2O + \frac{1}{4}O_2 \rightarrow Cu^{2+} - OH$ |
| **Sum:** | $\mathbf{NO + \frac{1}{2}O_2 \rightarrow NO_2}$ |

**Table 5**
Linear reaction combination that simulates NO oxidation.

| | |
|---|---|
| **2*R12** | $4Cu^{2+} - OH + 2NO \leftrightarrow 2Cu^{2+} - ONO + 2H_2O + 2Cu^+$ |
| **R2r + R3r** | $Cu^{2+} - ONO + Cu^{2+} - NO_3 + H_2O \leftrightarrow 2NO_2 + 2Cu^{2+} - OH$ |
| **R4** | $NO_2 + Cu^{2+} - ONO \leftrightarrow Cu^{2+} - NO_3 + NO$ |
| **2*R13** | $2Cu^+ + H_2O + \frac{1}{2}O_2 \rightarrow 2Cu^{2+} - OH$ |
| **Sum:** | $\mathbf{NO + \frac{1}{2}O_2 \rightarrow NO_2}$ |

**Table 6**
Linear reaction combination that simulates NO₂ decomposition.

| | |
|---|---|
| **2*R14r** | $2NO_2 + 2Cu^{2+} - OH \leftrightarrow 2Cu^{2+} - ONO + H_2O + \frac{1}{2}O_2$ |
| **R2r + R3r** | $Cu^{2+} - ONO + Cu^{2+} - NO_3 + H_2O \leftrightarrow 2NO_2 + 2Cu^{2+} - OH$ |
| **R4** | $NO_2 + Cu^{2+} - ONO \leftrightarrow Cu^{2+} - NO_3 + NO$ |
| **Sum:** | $\mathbf{NO_2 \leftrightarrow NO + \frac{1}{2}O_2}$ |

mechanisms were not investigated here, the re-oxidation of $Cu^+$ *via* oxygen (R13) was parameterised so that it is never rate limiting, and despite this simplifying assumption, simulates the Standard SCR steady state points well. Additionally, the influence of different oxygen concentrations was not investigated in this work and a constant 6% oxygen was used in all experiments.

NO oxidation is proposed to proceed *via* a nitrite intermediate (Table 4): R12, the linking reaction between NO oxidation and Standard SCR, is first responsible for the formation of nitrites; this is followed by the oxidation of nitrites to $NO_2$ (R14) and the re-oxidation of $Cu^+$ (R13) [16].

The pre-exponential factors and activation energies of reactions R12, R6, and R14, were fit using steady state Standard SCR and NO oxidation experiments; the experimental data and resulting kinetic fit for NO oxidation, $NO_2$ decomposition, and a mixed feed of NO and $NO_2$ are shown in Fig. 5. Surprisingly, the reaction mechanism in Table 4 was not solely responsible for the simulation of NO oxidation, where an alternative active linear combination of reactions describing NO oxidation is shown in Table 5. The difference between the mechanisms in Tables 4 and 5 is how the nitrites are oxidized, where the nitrites are oxidized via nitrates in Table 5 (R2r + R3r), rather than oxygen in Table 4 (R14). While the mechanism in Table 5 was found to be dominant for NO oxidation, it required $NO_2$ to proceed, which is first formed via the NO oxidation reaction in Table 4.

Since the oxidation of $Cu^+$ (R13) is assumed to be irreversible, the mechanistic pathways shown in Tables 4 and 5 do not describe $NO_2$ decomposition. Nevertheless, $NO_2$ decomposition is described by a different linear combination of reactions in Table 6, where copper always remains in its oxidized form ($Cu^{2+}$).

Fig. 6 shows the experimental data and resulting kinetic fit for the Standard SCR experiment, where a constant feed gas of 550 ppm $NH_3$, 500 ppm NO, 5% $H_2O$, and 6% $O_2$, with $N_2$ balance gas flowed through the catalytic converter sample. The catalyst allows for complete NO conversion and 90% ammonia conversion between 250 and 300 °C; as the temperature is increased further, the ammonia conversion continues to increase while the NO conversion decreases, owing to ammonia oxidation (discussed in Section 4.4). $N_2O$ formation increases until 225 °C, where it then starts to decrease, followed by an increase at 500 °C.

The model captures the Standard SCR light-off and ammonia oxidation above 400 °C. The $N_2O$ formation below 400 °C is accounted by R7; however, the high temperature $N_2O$ formation due to unselective Standard SCR to $N_2O$ is not modelled. The addition of a second

**Fig. 6.** Comparison of experimental (dots) and simulated (lines) concentrations for Standard SCR; Feed = 550 ppm $NH_3$, 500 ppm NO, 5% $H_2O$, 6% $O_2$, and $N_2$ balance gas; GHSV at STP = 50,000 $h^{-1}$.

ammonia adsorption site would help capture such an increase. The reaction parameters of R6, R7, R12, and R14 were optimized to steady state NO oxidation, $NO_2$ decomposition, and Standard SCR data points simultaneously.

### 4.4. Ammonia oxidation

Steady state measurements with a feed of 500 ppm $NH_3$ were completed to collect ammonia oxidation steady state data points. The resulting experimental points and modelling fit are shown in Fig. 7.

As seen in Fig. 7, ammonia oxidation over the catalyst is almost completely selective to nitrogen, with only minor amounts of NO and $N_2O$ being produced. To describe the ammonia oxidation selectivity to NO and $N_2O$, reactions R15 and R16 were implemented.

$$4NH_3^* + 5O_2 \rightarrow 4NO + 6H_2O + 4^* \tag{R15}$$

$$2NH_3^* + 2O_2 \rightarrow N_2O + 3H_2O + 2^* \tag{R16}$$

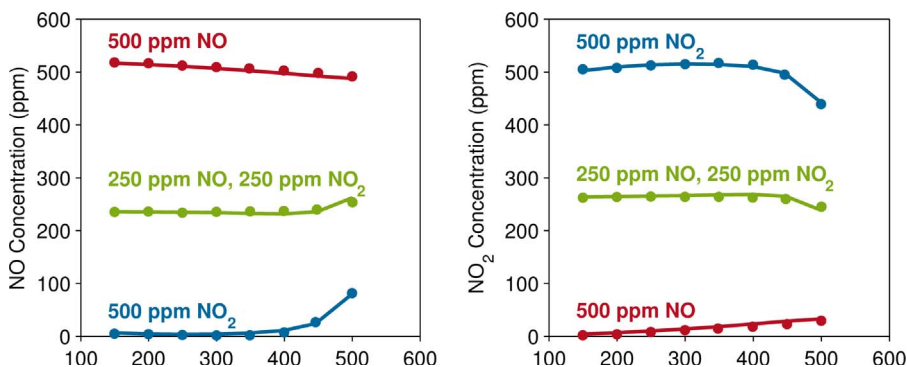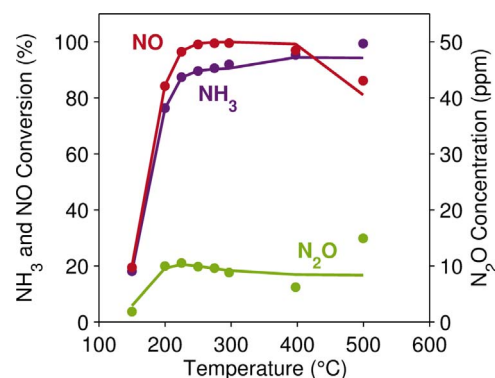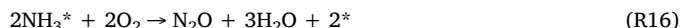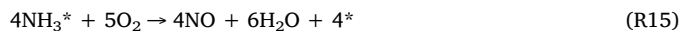**Fig. 5.** Comparison of experimental (dots) and simulated (lines) concentrations for NO oxidation, $NO_2$ decomposition, and NO/$NO_2$ reaction studies; Feed = varying NO/$NO_2$, 5% $H_2O$, 6% $O_2$, $N_2$ as Balance Gas; GHSV at STP = 50,000 $h^{-1}$.

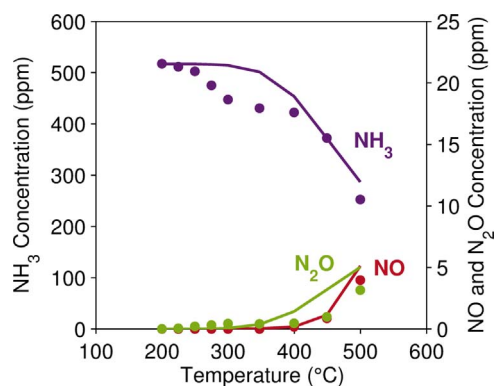**Fig. 7.** Comparison of experimental (dots) and simulated (lines) concentrations for ammonia oxidation; Feed = 550 ppm $NH_3$, 5% $H_2O$, 6% $O_2$, and $N_2$ balance gas; GHSV at STP = 50,000 $h^{-1}$.

The need to implement a reaction for ammonia oxidation to $N_2$ was unnecessary, as it is already being described through the combination of Standard SCR (1) and ammonia oxidation to NO (R15). Additionally, like in the work of Olsson et al. [27] and Gao et al. [36], the chabazite catalyst displayed two regions of active ammonia oxidation. Gao et al. [36] suggests this could either be a change in rate limiting mechanism or a change in Cu catalytic centres. Olsson et al. [27] successfully modelled this effect with two active sites. Given that only one active site is being used for ammonia storage in this work, ammonia oxidation was only fit to the higher temperature points, resulting in ammonia oxidation not being modelled at lower temperatures.

### 4.5. Fast SCR

To fit the reaction mechanism to model Fast SCR, steady state experiments were completed for these reactions. A feed of 550 ppm $NH_3$, 250 ppm NO, 250 ppm $NO_2$, 5% $H_2O$, 6% $O_2$, and $N_2$ balance gas were passed through the catalytic converter, while the temperature was held constant at the desired points until the system had reached steady state. The steady state points are shown in Fig. 8**A**.

In this work, Fast SCR is modelled using the mechanism proposed by Grossale et al. [24,25,6]; according to the mechanism, the active centre (i.e., $Fe^{3+}$ or $Cu^{2+}$) does not change oxidation state. This agrees with

**Table 7**
Linear reaction combination for Fast SCR.

| | |
|---|---|
| **2*R1** | $2NH_3 + 2* \leftrightarrow 2NH_3*$ |
| **R2 + R3** | $2NO_2 + 2Cu^{2+} - OH \leftrightarrow Cu^{2+} - ONO + Cu^{2+} - NO_3 + H_2O$ |
| **R4r** | $Cu^{2+} - NO_3 + NO \leftrightarrow NO_2 + Cu^{2+} - ONO$ |
| **2*R6** | $2Cu^{2+} - ONO + 2NH_3* \rightarrow 2N_2 + 2H_2O + 2Cu^{2+} - OH + 2*$ |
| **Sum:** | $\mathbf{2NH_3 + NO + NO_2 \rightarrow 2N_2 + 3H_2O}$ |

the work of McEwan et al. [35], who concluded that only $Cu^{2+}$ is present under Fast and $NO_2$ SCR conditions. Fast SCR mechanisms have been proposed where the active centre changes oxidation state [23,37], but were not tested in this work. The global Fast SCR mechanism is implemented *via* the linear combination of reactions in Table 7.

Since the kinetic parameters of these equations have already been fit to the $NO_2$ adsorption and Standard SCR experiments, they were applied directly to simulate the steady state Fast SCR data. However, applying the above mechanism directly with the aforementioned tuned parameters initially resulted in the Fast SCR activity being too high at 150 °C and 200 °C (not shown here), despite R4r being the rate limiting step, indicating that another reaction or effect must be hindering the mechanism. Research by Grossale et al. [34] found that the addition of ammonia at low temperatures hinders nitrates from reacting with NO *via* R4r, and explained the decrease of Fast SCR activity through "ammonia blocking" species, which represent the strong interaction between adsorbed nitrates and ammonia at low temperatures. This effect was later included in a model for $NO_2$ SCR related chemistry by Colombo et al. [6] as $Cu^{2+}$-$NO_3[NH_3]$ species, and was partially responsible for $N_2O$ formation, along with ammonium nitrate.

Inclusion of $Cu^{2+}$-$NO_3[NH_3]$ species in our mechanism *via* R9 allows for the simulation of the experimental activity at 150 and 200 °C, and is also responsible for the $N_2O$ formation during Fast SCR (R10) shown in Fig. 8**A**. The simulation predicts the experimental steady state conversions well, however, the $NH_3$ and NO conversions are over-predicted between 225 and 300 °C during Fast SCR, because R12 (for Standard SCR) is too active. Fig. 8**B** shows the simulated average surface coverage of the $Cu^{2+}$-$NO_3[NH_3]$, $NH_3*$, and $NH_4NO_3*$ species. The $NH_4NO_3*$ species formation, resulting from a $Cu^{2+}$-$NO_3[NH_3]$ spill-over effect on ammonia storage sites (*) *via* R11, will be described in detail in Section 4.7.

### 4.6. $NO_2$ SCR over Cu-free Chabazite

Interestingly, during the model development process, it was observed that the zeolite itself, and not copper, is mainly responsible for the low temperature (T < 250 °C) $NO_2$ SCR steady state conversion over Cu-CHA. This conclusion was drawn based on the comparison of $NO_2$ SCR steady state experiments over a Cu-free CHA (Fig. 9) catalyst



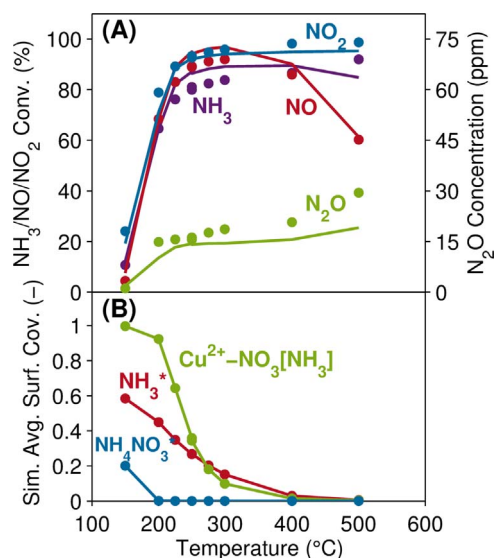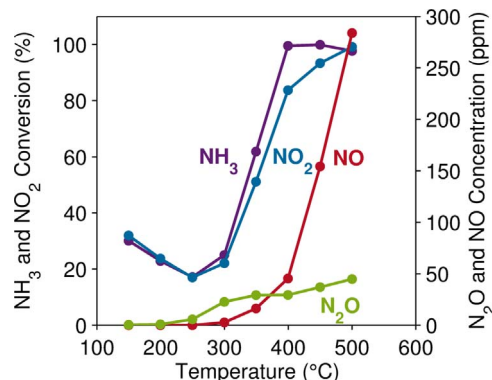**Fig. 8.** (A) Comparison of experimental (dots) and simulated (lines) concentrations for Fast SCR; Feed = 550 ppm $NH_3$, 250 ppm NO, 250 ppm $NO_2$, 5% $H_2O$, 6% $O_2$, and $N_2$ balance gas; GHSV at STP = 125,000 $h^{-1}$. (B) Simulated average surface coverage of species.



**Fig. 9.** Experimental concentrations for $NO_2$ SCR over Cu-free chabazite (78% of the zeolite of Cu-CHA, aged 50 °C lower than Cu-CHA); Feed = 550 ppm $NH_3$, 500 ppm $NO_2$, 5% $H_2O$, 6% $O_2$, and $N_2$ balance gas; GHSV at STP = 50,000 $h^{-1}$.

versus a Cu-CHA catalyst (Fig. 12A), where the Cu-free CHA had 78% of the zeolite content of the Cu-CHA catalyst, and was aged at a slightly different temperature. The catalysts showed a similar conversion below 250 °C, while Cu-CHA was more active than Cu-free CHA above 250 °C, indicating that the copper played an active role in the steady state $NO_2$ SCR conversion at higher temperatures.

The reason for the low temperature activity over Cu-free CHA could be owing to a reaction between adsorbed $NO_2$ and $NH_3$. Our $NO_2$ adsorption experiments over Cu-free CHA (not shown) indicated that $NO_2$ is adsorbed by the zeolite, which has also been observed over Cu-free ZSM-5 [38], and is supported by the possible formation of $NO^+$ on zeolites [39,40]. However, as the detailed investigation of reaction mechanisms on the zeolite is out of the scope of this work, R18 was added as a global reaction to describe the high conversion of ammonia and $NO_2$ to $N_2$ at low temperatures.

$$2NH_3^* + 2NO_2 \rightarrow 2N_2 + 3H_2O + \tfrac{1}{2}O_2 + 2^* \qquad (R18)$$
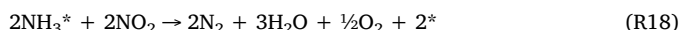
Reaction R18 was fit to the transient experiments shown in Section 4.7. However, the importance of this reaction is already seen during Fast SCR experiments (Fig. 8), where R18 ensures that the $NH_3$ and $NO_2$ conversion is captured, although the copper sites are completely blocked with $Cu^{2+}$-$NO_3$[$NH_3$].

Finally, it is important to note that, throughout all experiments shown in this work, the tubing from the reactor to the FTIR was heated to prevent ammonium nitrate deposition in the tubes. When adding ammonia and $NO_2$ at a constant temperature of 150 °C with an empty reactor, an approximate 3–4% constant steady state conversion is seen (not shown), indicating that the $NH_3$ and $NO_2$ experimental conversion with a reactor may be minimally overpredicted at this temperature.

### 4.7. $NO_2$ SCR over Cu-CHA

The $NO_2$ SCR reaction mechanism was investigated via both transient temperature programmed surface reaction (TPSR) and stationary experiments. The TPSR experiments were completed at 150 and 200 °C, where the experimental and simulated results, along with simulated surface coverages, are shown in Figs. 10 and 11. In these experiments, $NO_2$ SCR conditions (500 ppm $NH_3$ and 500 ppm $NO_2$) were first passed through the catalytic converter at a fixed adsorption temperature, to investigate transients that occur when $NH_3$ and $NO_2$ are added simultaneously at low temperatures. The significant transients seen during the ammonia and $NO_2$ addition can be explained as follows:

1. $NO_2$ storage and breakthrough (Fig. 10, 0–200 s): Initially, $NO_2$ is consumed and stored in the form of nitrates ($Cu^{2+}$-$NO_3$), leading to NO production, owing to the $NO_2$ adsorption dynamics (R2-R4, Section 4.2). The $NO_2$ breakthrough increases and NO production decreases because the $NO_2$ and nitrates reach an equilibrium.

2. Consumption of $NO_2$ owing to availability of stored ammonia (Fig. 10, 200–800 s): Once the stored ammonia becomes available, it reacts with the nitrites and nitrates formed via $NO_2$ adsorption, resulting in a decrease in the $NO_2$ outlet concentration. The reaction between ammonia and nitrates allows for the formation of $Cu^{2+}$-$NO_3$[$NH_3$] (R9), which allows for the subsequent formation of $NH_4NO_3^*$ discussed momentarily (R11), while the reaction between ammonia and nitrites (R6) causes a peak in nitrogen production.

3. Breakthrough of $NO_2$ and $NH_3$ (Fig. 10, 800–6800s): As the surface species $NH_4NO_3^*$ slowly approaches steady state, the consumption of the $Cu^{2+}$-$NO_3$[$NH_3$] intermediate decreases (R11), resulting in less ammonia and $NO_2$ consumption. Therefore, the outlet concentration of ammonia and $NO_2$ increases and slowly reaches steady state. Despite the complete blocking of the copper sites with $Cu^{2+}$-$NO_3$[$NH_3$], a constant conversion of ammonia and $NO_2$ is seen during steady state conditions owing to the reaction between ammonia and $NO_2$ taking place on the ammonia adsorption sites (R18, Section 4.6).

From a modelling perspective, we have already added the reactions responsible for describing the $NO_2$ adsorption dynamics required for Step #1, along with the reactions occurring between ammonia and nitrates to build $Cu^{2+}$-$NO_3$[$NH_3$] (R9) and ammonia and nitrites to produce nitrogen (R6) for Step #2. However, if no further reactions were to be implemented, and $Cu^{2+}$-$NO_3$[$NH_3$] were the only inhibiting species formed via R9 in Step #2, all copper sites would be blocked with $Cu^{2+}$-$NO_3$[$NH_3$] too quickly ($\sigma_{NO3NH3} = 1$). As a result, ammonia and $NO_2$ would break through immediately, because no more $NO_2$ could adsorb on the copper via nitrates and nitrates (R2/R3), and react with the stored ammonia (R9/R11). Thus, the slow, transient breakthrough of $NO_2$ and ammonia in Step #3 would not be modelled. To avoid this and capture the slow dynamics of ammonia and $NO_2$ at low temperatures, an ammonium nitrate spill-over effect was included as R11; during this reaction, the ammonium nitrate-like species formed on the copper site can be adsorbed on the ammonia storage site as ammonium nitrate ($NH_4NO_3^*$), freeing a copper site for further reaction.
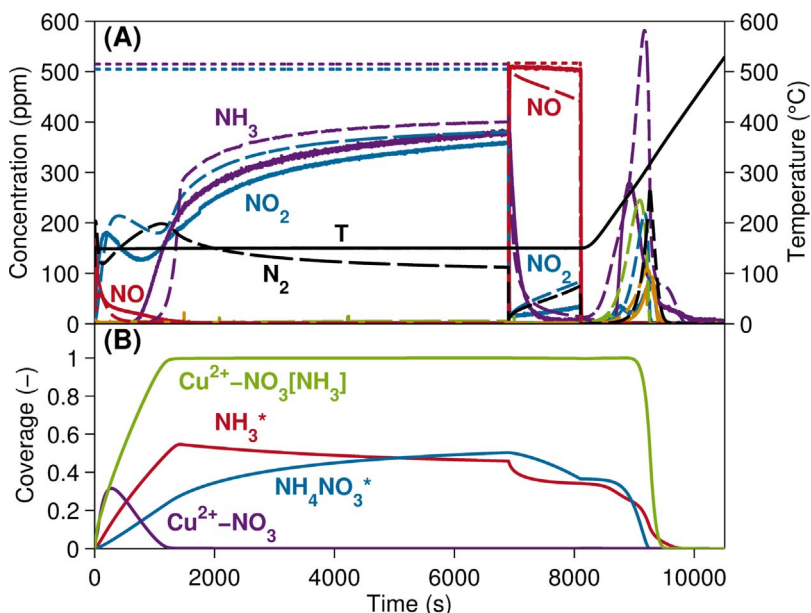


Fig. 10. (A) Comparison of experimental (solid lines) and simulated (dashed lines) concentrations for $NH_3$ + $NO_2$ then NO during constant adsorption temperature of 150 °C; Feed (dotted lines) = 500 ppm $NH_3$ and $NO_2$, followed by 500 ppm NO. 5% $H_2O$, 6% $O_2$, and $N_2$ balance gas always present in feed; GHSV at STP = 50,000 $h^{-1}$. (B) Simulated average surface coverage of species.

**Fig. 11.** (A) Comparison of experimental (solid lines) and simulated (dashed lines) concentrations for $NH_3$ + $NO_2$ then NO during constant adsorption temperature of 200 °C; Feed (dotted lines) = 500 ppm $NH_3$ and $NO_2$, followed by 500 ppm NO. 5% $H_2O$, 6% $O_2$, and $N_2$ balance gas always present in feed; GHSV at STP = 50,000 $h^{-1}$. (B) Simulated average surface coverage of species.
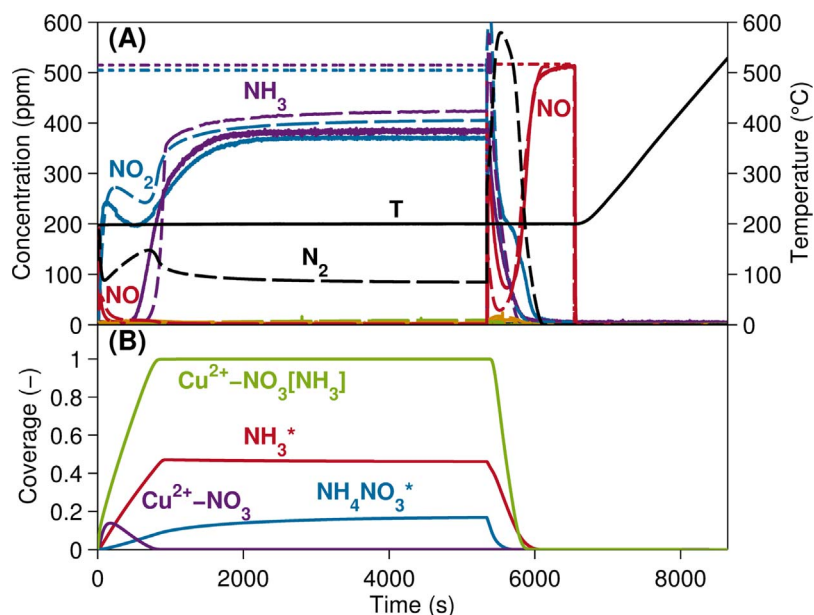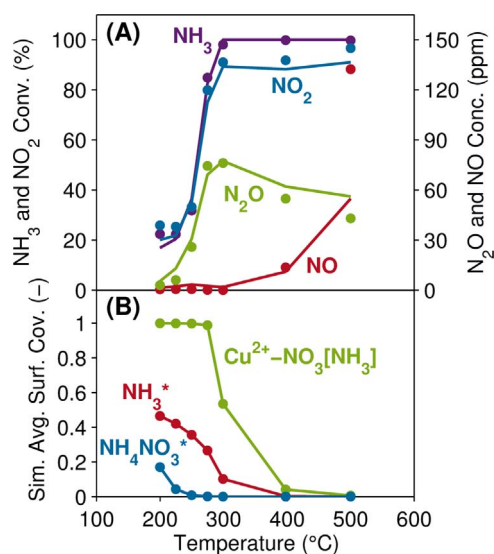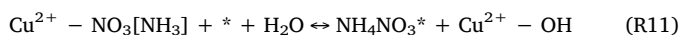


**Fig. 12.** (A) Comparison of experimental (dots) and simulated (lines) concentrations for $NO_2$ SCR; Feed = 550 ppm $NH_3$, 500 ppm $NO_2$, 5% $H_2O$, 6% $O_2$, and $N_2$ balance gas; GHSV at STP = 50,000 $h^{-1}$. (B) Simulated average surface coverage of species.

$$Cu^{2+} - NO_3[NH_3] + * + H_2O \leftrightarrow NH_4NO_3* + Cu^{2+} - OH \qquad (R11)$$

Interestingly, it does not appear that the $Cu^{2+}$-$NO_3[NH_3]$ and $NH_4NO_3*$ species play a significant inhibitive role during a transient driving cycle. The simulation of an 1800s WHTC driving cycle with a high $NO_2/NO_x$ ratio in Section 4.8 will show that only a maximum predicted 6% $Cu^{2+}$-$NO_3[NH_3]$ species, and no $NH_4NO_3*$ species, are formed on the catalyst surface. From a modelling perspective, this indicates the importance of capturing the dynamics at the beginning of the TPSR experiments (i.e., Steps #1, 2), compared to the steady state conditions at the end (Step #3).

It is well-known that the addition of NO allows for ammonium nitrate decomposition [5,29,34]. To investigate this effect, and see whether it is described by our model, ammonia and $NO_2$ was eliminated from the feed in the experiments shown in Figs. 10 and 11, while 500 ppm NO was added to allow for ammonium nitrate decomposition. The addition of NO allowed for minimal decomposition of $Cu^{2+}$-$NO_3[NH_3]$ (R9) and $NH_4NO_3*$ (R11) at 150 °C (Fig. 10, 6800–8000s), while all ammonium nitrate-likes species decomposed through the NO

addition at 200 °C (Fig. 11, 5500–6500s), in line with observations over a Cu-zeolite [29] and Fe-zeolite catalyst [34]. Thereafter, NO was removed from the feed and was followed by a 10 K/min temperature ramp, which was completed to verify whether any species remained on the catalyst surface (Fig. 10, 8000–10,000 s). Species desorbed during the TPSR at 150 °C, owing to $Cu^{2+}$-$NO_3[NH_3]$, $NH_4NO_3*$, and ammonia storage, whereas no surface species were left to desorb during the 200 °C experiment.

The decomposition of $Cu^{2+}$-$NO_3[NH_3]$ and $NH_4NO_3*$ through the addition of NO to the feed is modelled well, without the need of any additional reactions added to the mechanism. The decomposition reaction has been proposed to proceed *via* the global reaction shown in Table 8 [5], and is modelled by a linear combination of our mechanistic reactions. This mechanism largely reflects the mechanism proposed in reference [29], apart from the "spill-over" reaction (R11) used to capture the inhibiting formation of ammonium nitrate on the ammonia adsorption sites.

Following an adsorption temperature of 150 °C (Fig. 10), the amount of the species desorbed during the TPD is simulated to be too high, despite the correct qualitative trends, indicating that too much ammonium nitrate is predicted to be stored. Both the experiments and simulation did not have any species available to desorb during the TPD following an adsorption temperature of 200 °C.

For the stationary $NO_2$ SCR experiments, 550 ppm $NH_3$ and 500 ppm $NO_2$ were passed through the monolith, with the experimental results and simulated fit appearing in Fig. 12A. In this experiment, the presented mechanism thus far would already predict the low temperature $NH_3$ and $NO_2$ conversions (< 250 °C), owing to the addition of R18 taking place on the zeolite, along with the $N_2O$ formation due to $Cu^{2+}$-$NO_3[NH_3]$ species decomposition (R10). However, the reaction mechanism presented until now would incorrectly predict the light-off curve, as a reaction between nitrates and ammonia, leading to nitrogen formation, needs to be added to describe the main $NO_2$ SCR reaction. Therefore, R8 was added, allowing us to model $NO_2$ SCR according to a

**Table 8**
Linear reaction combination for decomposition of $NH_4NO_3$ via NO.

| | |
|---|---|
| **R11r** | $NH_4NO_3* + Cu^{2+} - OH \leftrightarrow Cu^{2+} - NO_3[NH_3] + * + H_2O$ |
| **R9r** | $Cu^{2+} - NO_3[NH_3] + * \leftrightarrow Cu^{2+} - NO_3 + NH_3*$ |
| **R4r** | $Cu^{2+} - NO_3 + NO \leftrightarrow NO_2 + Cu^{2+} - ONO$ |
| **R6** | $Cu^{2+} - ONO + NH_3* \rightarrow N_2 + H_2O + Cu^{2+} - OH + *$ |
| **Sum:** | $\mathbf{NH_4NO_3* + NO \rightarrow NO_2 + N_2 + 2H_2O + *}$ |

**Table 9**
Linear reaction combination for $NO_2$ SCR.

| 8*R1 | $8NH_3 + 8* \leftrightarrow 8NH_3*$ |
|---|---|
| 3*(R2+R3) | $6NO_2 + 6Cu^{2+} - OH \leftrightarrow 3Cu^{2+} - ONO$ |
| | $\quad + 3Cu^{2+} - NO_3 + 3H_2O$ |
| 6*R6 | $6Cu^{2+} - ONO + 6NH_3* \rightarrow 6N_2 + 6H_2O + 6Cu^{2+} - OH + 6*$ |
| R8 | $3Cu^{2+} - NO_3 + 2NH_3* \rightarrow 3Cu^{2+} - ONO + N_2 + 3H_2O + 2*$ |
| **Sum:** | $\mathbf{8NH_3 + 6NO_2 \rightarrow 7N_2 + 12H_2O}$ |

**Table 10**
Linear reaction combination for $NO_2$ SCR to NO.

| 2*R1 | $2NH_3 + 2* \leftrightarrow 2NH_3*$ |
|---|---|
| R2+R3 | $2NO_2 + 2Cu^{2+} - OH \leftrightarrow Cu^{2+} - ONO + Cu^{2+} - NO_3 + H_2O$ |
| R4 | $NO_2 + Cu^{2+} - ONO \leftrightarrow Cu^{2+} - NO_3 + NO$ |
| R17 | $2Cu^{2+} - NO_3 + 2NH_3* \rightarrow N_2 + 2NO + 2H_2O + 2Cu^{2+} - OH + 2*$ |
| **Sum:** | $\mathbf{2NH_3 + 3NO_2 \rightarrow N_2 + 3NO + 3H_2O}$ |

mechanism proposed by Grossale et al. that is presented in Table 9 [26,6]. Additionally, since a significant amount of NO forms at high temperatures, an unselective $NO_2$ SCR to NO reaction has also been added and its linear combination is shown in Table 10.

Reactions R8, R9, R10, and R17 were fit to both the Fast SCR and $NO_2$ SCR experiments simultaneously. The $NO_2$ SCR fit (Fig. 12) is excellent, with the exception that the NO produced at 500 °C during $NO_2$ SCR is underpredicted. Increasing the activity of $NO_2$ SCR to NO *via* R17 with the current parameter set causes over-production of NO at 500 °C during Fast SCR.

### 4.8. Predictive simulation of driving cycle

In a final step, we applied the kinetic model to a driving cycle without refitting of parameters, verified its performance, and looked at the simulated surface species formed. A WHTC driving cycle with a high $NO_2/NO_x$ ratio, i.e. a high rate of $NO_2$ formation in the DOC, was selected since it had the potential for a greater ammonium nitrate

formation and activity inhibition. No ammonia was initially stored on the catalyst and, rather than a cold start, the initial temperature of the WHTC driving cycle was 200 °C. The inlet conditions, along with the experimental and simulated output for $NO_x$ and $N_2O$ are shown in Fig. 13. The simulation of the driving cycle using the presented mechanistic model allowed for the prediction of the NO, $NO_2$, and $N_2O$ cumulated emissions.

A plot of the simulated surface coverage is shown in Fig. 14. Here, it is seen that only a maximum of 8% ammonium blocking species ($Cu^{2+}$-$NO_3[NH_3]$) are predicted to inhibit the copper active sites over the driving cycle. No nitrates ($Cu^{2+}$-$NO_3$) and no ammonium nitrate ($NH_4NO_3*$) on the ammonia storage sites are predicted to form. As the temperature increases towards the end of the driving cycle, the ammonium blocking species decreases, meaning they will no longer play an inhibitive role at the end of the cycle.

The surface coverages throughout the driving cycle (Fig. 14) vary significantly from the predicted surface coverages at steady state conditions (Figs. 8 **B**, 12 **B**). Clearly, a model that assumes steady state for the nitrate species and is calibrated based on only steady state data, would not be able to predict the transient conversion correctly. This emphasizes the importance of modelling transient effects (i.e., ammonia storage, nitrites, and nitrates) to capture the dynamics during driving cycles, since steady state conditions are not reached.

### 5. Conclusions

In this work, a surface reaction mechanism was developed by integrating various mechanistic pathways proposed in literature. The presented mechanism describes the main SCR reactions (Standard SCR, Fast SCR, $NO_2$ SCR) as well as transient effects due to nitrate storage. A dual site approach was used, where site 1 accounts for the adsorbed ammonia on Brønsted acid and copper ions, while site 2 represents a copper ion ($Cu^{2+}$-OH) where nitrates and nitrites could form.

All main SCR reactions proceed *via* a reaction between ammonia and nitrites (ammonium nitrite pathway) to produce nitrogen; the nitrites are also modelled to be the linking species between the Standard
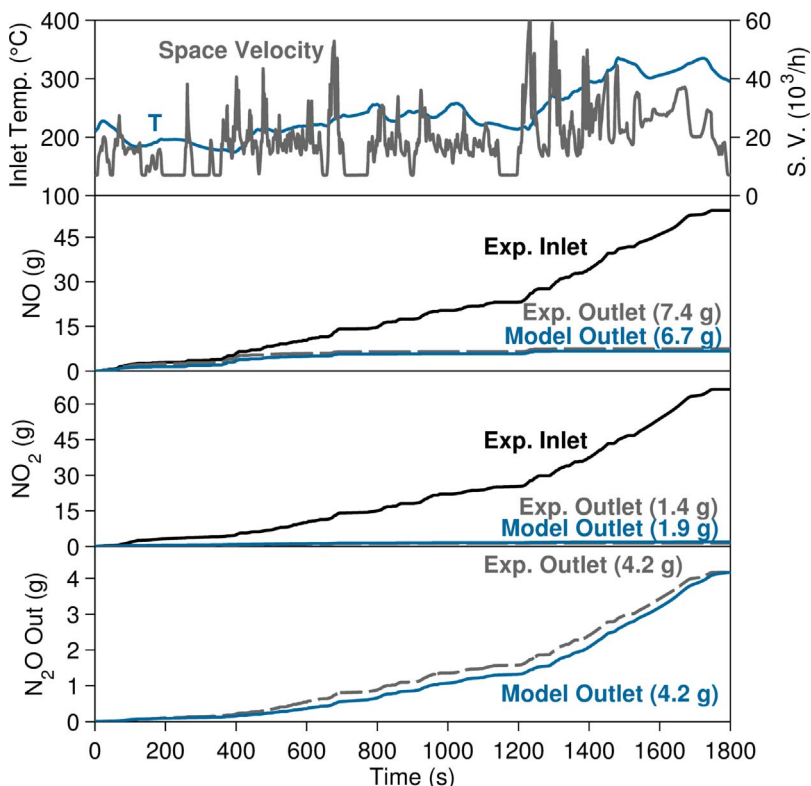


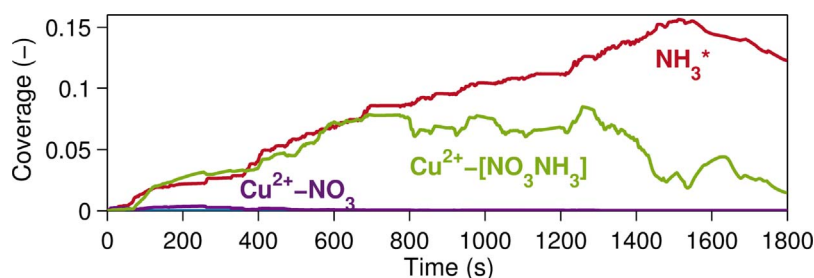**Fig. 13.** Predictive simulation of WHTC driving cycle.

**Fig. 14.** Predicted surface coverage for WHTC driving cycle.

SCR and NO oxidation reactions. Ammonium nitrate formation and decomposition effects were included in the model, in addition to a low temperature (< 250 °C) global reaction that was observed to take place between $NH_3$ and $NO_2$ on the zeolite catalyst.

The reaction parameters were fit to steady state and transient experiments and predict the behaviour of the catalyst during a driving cycle, without any refitting of kinetic parameters required. The surface coverages of ammonium nitrate-like species ($Cu^{2+}$-$NO_3[NH_3]$, $NH_4NO_3$*) throughout the driving cycle were significantly less than during the Fast and $NO_2$ SCR steady state experiments. Thus, if we would have fit to only steady state data, we would have assumed a substantial amount of steady state surface species, and incorrectly predicted the transient, driving cycle conversion. This observation emphasizes the importance of modelling transient behaviour rather than steady state activity for the simulation of driving cycles. The minimal formation of nitrate species during the driving cycle, however, does not necessarily imply that nitrate or ammonium nitrate effects do not play a role during other driving scenarios with longer periods of low temperature operation that might occur during real world driving.

Finally, this paper shows that the current mechanistic understanding of the different SCR subreactions forms a useful basis for the construction of a kinetic model that describes and predicts the behaviour of the copper chabazite catalyst under realistic operating conditions. However, it needs to be emphasized that most of the individual submechanisms used in this work are not settled and still under investigation. Nevertheless, we believe that the individual mechanisms should be integrated into comprehensive models at an early stage. This not only leads to a better understanding of the transient catalyst behaviour, but also contributes to the discussion of the individual submechanisms, as it helps to understand their role and importance in the overall reaction system.

## Acknowledgments

## References

[1] I. Nova, E. Tronconi (Eds.), Urea-SCR Technology for DeNOx After Treatment of Diesel Exhausts, Springer, 2014.

[2] M. Koebel, M. Elsener, M. Kleeman, Urea-SCR: a promising technique to reduce NOx emissions from automotive diesel engines, Catal. Today 59 (2000) 335–345.

[3] M. Colombo, I. Nova, E. Tronconi, A comparative study of the NH3-SCR reactions over a Cu–zeolite and a Fe–zeolite catalyst, Catal. Today 151 (2010) 223–230.

[4] A. Schuler, M. Votsmeier, P. Kiwic, J. Gieshoff, W. Hautpmann, A. Drochner, H. Vogel, NH3-SCR on Fe zeolite catalysts − from model setup to NH3 dosing, Chem. Eng. J. 154 (2009) 333–340.

[5] H.-Y. Chen, Z. Wei, M. Kollar, F. Gao, Y. Wang, J. Szanyi, C.H.F. Peden, A comparative study of N2O formation during the selective catalytic reduction of NOx with NH3 on zeolite supported Cu catalysts, J. Catal. 329 (2015) 490–498.

[6] M. Colombo, I. Nova, E. Tronconi, NO2 adsorption on Fe- and Cu-zeolite catalysts: the effect of the catalyst red-ox state, Appl. Catal. B 111–112 (2012) 433–444.

[7] J. Jansson, Vanadia-Based catalysts for mobile SCR, in: I. Nova, E. Tronconi (Eds.), Urea-SCR Technology for DeNOx After Treatment of Diesel Exhausts, Springer, 2014, pp. 65–96.

[8] D.W. Fickel, E. D'Addio, J.A. Lauterbach, R.F. Lobo, The ammonia selective catalytic reduction activity of copper-exchanged small-pore zeolites, Appl Catal. B 102 (2011) 441–448.

[9] A.M. Beale, F. Gao, I. Lezcano-Gonzalez, C.H.F. Peden, J. Szanyi, Recent advances in automotive catalysts for NOx emission control by small-pore microporous materials, Chem. Soc. Rev. 44 (2015) 7371.

[10] F. Gao, E.D. Walter, M. Kollar, Y. Wang, J. Szanyi, C.H.F. Peden, Understanding ammonia selective catalytic reduction kinetics over Cu/SSZ-13 from motion of Cu ions, J. Catal. 319 (2014) 1–14.

[11] S.A. Bates, A.A. Verma, C. Paolucci, A.A. Parekh, T. Anggara, A. Yezerets, W.F. Schneider, J.T. Miller, W.N. Delgass, F.H. Ribeiro, Identification of the active Cu site in standard selective catalytic reduction with ammonia on Cu-SSZ-13, J. Catal. 312 (2014) 87–97.

[12] A.A. Verma, S.A. Bates, T. Anggara, C. Paolucci, A.A. Parekh, K. Kamasamudram, A. Yezerets, J.T. Miller, W.N. Delgass, W.F. Schneider, F.H. Ribeiro, NO oxidation: a probe reaction on Cu-SSZ-13, J. Catal. 312 (2014) 179–190.

[13] H. Zhu, J.H. Kwak, C.H.F. Peden, J. Szanyi, In situ DRIFTS-MS studies on the oxidation of adsorbed NH3 by NOx over a Cu-SSZ-13 zeolite, Catal. Today 205 (2013) 16–23.

[14] I. Lezcano-Gonzalez, U. Deka, B. Arstad, A. Van Yperen-De Deyne, K. Hemelsoet, M. Waroquier, V. Van Speybroeck, B.M. Weckhuysen, A.M. Beale, Determining the storage availability, and reactivity of NH3 within Cu-Chabazite-based Ammonia Selective Catalytic Reduction systems, Phys. Chem. Chem. Phys. 16 (2014) 1639–1650.

[15] S. Brandenberger, O. Kroecher, A. Tissler, R. Althoff, P.D. Schettler, The state of the art in selective catalytic reduction of NOx by ammonia using metal-exchanged zeolite catalysts catalysis reviews, Sci. Eng. 50 (2008) 492–531.

[16] M.P. Ruggeri, T. Selleri, M. Colombo, I. Nova, E. Tronconi, Identification of nitrites/HONO as primary products of NO oxidation over Fe-ZSM-5 and their role in the Standard SCR mechanism: a chemical trapping study, J. Catal. 311 (2014) 266–270.

[17] M.P. Ruggeri, I. Nova, E. Tronconi, J.A. Pihl, T.J. Toops, W.P. Partridge, In-situ DRIFTS measurements for the mechanistic study of NO oxidation over a commercial Cu-CHA catalyst, Appl. Catal. B 166–167 (2015) 181–192.

[18] M.P. Ruggeri, T. Selleri, I. Nova, E. Tronconi, J.A. Pihl, T.J. Toops, W.P. Partridge, New mechanistic insights in the NH3-SCR reactions at low temperature, Top. Catal. 59 (2016) 907–912.

[19] J.H. Kwak, J.H. Lee, S.D. Burton, A.S. Lipton, C.H.F. Peden, J. Szanyi, A common intermediate for N2 formation in enzymes and zeolites: side-On Cu-nitrosyl complexes, Angew. Chem. Int. Ed. 52 (2013) 9985–9989.

[20] F. Gao, J.H. Kwak, J. Szanyi, C.H.F. Peden, Current understanding of Cu-exchanged chabazite molecular sieves for use as commercial diesel engine DeNOx catalysts, Top. Catal. 56 (2013) 1441–1459.

[21] C. Paolucci, A.A. Verma, S.A. Bates, V.F. Kispersky, J.T. Miller, R. Gounder, W.N. Delgass, F.H. Ribeiro, W.F. Schneider, Isolation of the copper redox steps in the standard selective catalytic reduction of Cu-SSZ-13, Angew. Chem. Int. Ed. 53 (2014) 11828–11833.

[22] T. Guenter, H.W.P. Carvalho, D.E. Doronkin, T. Sheppard, F. Glatzel, A.J. Atkins, J. Rudolph, C.R. Jacob, M. Casapu, J.-D. Grunwaldt, Structural snapshots of the SCR reaction mechanism on Cu-SSZ-13, Chem. Commun. 51 (2015) 9227–9230.

[23] T.V.W. Janssens, H. Falsig, L.F. Lundegaard, P.N.R. Vennestrom, S.B. Rasmussen, P.G. Moses, F. Giordanino, E. Borfecchia, K.A. Lomachenko, C. Lamberti, S. Bordiga, A. Godiksen, P. Mossin, P. Beato, A consistent reaction scheme for the selective catalytic reduction of nitrogen oxides with ammonia, ACS Catal. 5 (2015) 2832–2845.

[24] A. Grossale, I. Nova, E. Tronconi, D. Chatterjee, M. Weibel, The chemistry of the NO/NO2-NH3 fast SCR reaction over Fe-ZSM5 investigated by transient reaction analysis, J. Catal. 256 (2008) 312–322.

[25] M.P. Ruggeri, A. Grossale, I. Nova, E. Tronconi, H. Jirglova, Z. Sobalik, FTIR in situ mechanistic study of the NH3-NO/NO2 Fast SCR reaction over a commercial Fe-ZSM-5 catalyst, Catal. Today 184 (2012) 107–114.

[26] A. Grossale, I. Nova, E. Tronconi, Role of nitrate species in the NO2 SCR mechanism over a commercial Fe-zeolite catalyst for SCR mobile applications, Catal. Lett. 130 (2009) 525–531.

[27] L. Olsson, K. Wijayanti, K. Leistner, A. Kumar, S.Y. Joshi, K. Kamasamudram, N.W. Currier, A. Yezerets, A multi-site kinetic model for NH3-SCR over Cu/SSZ-13, Appl. Catal. B 174–175 (2015) 212–224.

[28] P. Metkar, M.P. Harold, V. Balakotaiah, Experimental and kinetic modeling study of NH3-SCR of NOx on Fe-ZSM-5, Cu-chabazite and combined Fe- and Cu-zeolite monolithic catalysts, Chem. Eng. Sci. 87 (2013) 51–66.

[29] M. Colombo, I. Nova, E. Tronconi, Detailed kinetic modeling of the NH3-NO/NO2 SCR reactions over a commercial Cu-zeolite catalyst for Diesel exhausts after treatment, Catal. Today 197 (2012) 243–255.

[30] E. Tronconi, P. Forzatti, Adequacy of lumped parameter models for SCR reactors with monolith structure, AlChE J. 38 (1992) 201–210.

[31] K.E. Brenan, S.L. Campbell, L.R. Petzold, Numerical Solution of Initial-value Problems in Differential-algebraic Equations, Elsevier Science Publishing Co, 1989.

[32] B. Opitz, M. Bendrich, A. Drochner, H. Vogel, R.E. Hayes, J.F. Forbes, M. Votsmeier, Simulation study of SCR catalysts with individually adjusted ammonia dosing strategies, Chem. Eng. J. 264 (2015) 936–944.

[33] A. Grossale, I. Nova, E. Tronconi, Study of a Fe–zeolite-based system as NH3-SCR catalyst for diesel exhaust aftertreatment, Catal. Today 136 (2008) 18–27.

[34] A. Grossale, I. Nova, E. Tronconi, Ammonia blocking of the "Fast SCR reactivity over a commercial Fe-zeolite catalyst for Diesel exhaust aftertreatment, J. Catal. 265 (2009) 141–147.

[35] J.-S. McEwen, T. Anggara, W.F. Schneider, V.F. Kispersky, J.T. Miller, W.N. Delgass, F.H. Ribeiro, Identification of the active Cu site in standard selective catalytic reduction with ammonia on Cu-SSZ-13, J. Catal. 312 (2014) 87–97.

[36] F. Gao, E.D. Walter, E.M. Karp, J. Luo, R.G. Tonkyn, J.H. Kwak, J. Szanyi, C.H.F. Peden, Structure-activity relationships in NH3-SCR over Cu-SSZ-13 as probed by reaction kinetics and EPR studies, J. Catal. 300 (2013) 20–29.

[37] L. Arnarson, H. Falsig, S.B. Rasmussen, J.V. Lauritsen, P.G. Moses, A complete reaction mechanism for standard and fast selective catalytic reduction of nitrogen oxides on low coverage VOx/TiO2(001) catalysts, J. Catal. 346 (2017) 188–197.

[38] L. Olsson, H. Sjoevall, R.J. Blint, Detailed kinetic modeling of NOx adsorption and NO oxidation over Cu-ZSM-5, Appl. Catal. B 87 (2009) 200–210.

[39] K. Hadjiivanov, J. Saussey, J.L. Freysz, J.C. Lavalley, FT-IR study of NO + O2 co-adsorption on H-ZSM-5: reassignment of the 2133 cm-1 band to NO+ species, Catal. Lett. 52 (1998) 103–108.

[40] J.A. Loiland, R.F. Lobo, Oxidation of zeolite acid sites in NO/O2 mixtures and the catalytic properties of the new site in NO oxidation, J. Catal. 325 (2015) 68–78.